Supporting Information

Zheng Ye[a], Chun Han[a], Yuan Yuan[a], Gong Chen[a], Yuanzun Fu[a], Yunhe Zhao[a, b]*

a. College of Chemistry, Chemical Engineering and Resource Utilization, Northeast Forestry University, 26 Hexing Road, Harbin, 150040, P. R. China.

b. Center for Innovative Research in Synthetic Chemistry and Resource Utilization, Northeast Forestry University, Harbin 150040, P. R. China.

*Corresponding author. *E-mail*: zhaoyunhe@nefu.edu.cn.

1. Experimental

1.1 Chemicals

Nickel nitrate hexahydrate ($Ni(NO_3)_2 \cdot 6H_2O$, 98%), urea ($CO(NH_2)_2$, 99%), ammonium fluoride (NH_4F, 98%), potassium ferricyanide ($K_3[Fe(CN)_6]$, 99%), phytic acid solution (PA, 60.3 wt% in water) and ethanol (C_2H_5OH 100%) were all of analytical grade and directly used in experiments without any treatment or further purification. All aqueous solutions were prepared using deionized (DI) water.

1.2 Pretreatment of nickel foam (NF)

Typically, the NF pieces were treated by ultrasonic in 1.0 M HCl solution, acetone solution, anhydrous ethanol and DI water, respectively. The HCl solution can remove the oxide layer on the surface of NF, and acetone can remove the organic impurities such as oil on its surface.

1.3 Synthesis of nickel hydroxide loaded on NF ($Ni(OH)_2$/NF)

The 1.5 mmol $Ni(NO_3)_2 \cdot 6H_2O$, 7.5 mmol urea and 3 mmol NH_4F were dissolved in 30 mL of DI water and stirred for 10 min to form a uniform solution system. Then a 50 mL polytetrafluoroethylene reactor was selected to fill the above mixed solution and immersed a piece of pretreated 1 × 2 cm^2 NF in it. The hydrothermal reaction temperature was controlled at 120 ℃ for 6 h. After being rinsed with water and ethanol, the sample was dried at 60 ℃ for 12 h to obtain $Ni(OH)_2$/NF.

1.4 Synthesis of transformed NiFe-PBA/NF (tPBA/NF)

The 3 mmol $K_3[Fe(CN)_6]$ was dispersed in a 30 mL mixed solvent (V_{water}: $V_{ethanol}$ = 2:1), followed by being stirred for 10 min to form a uniform yellow solution. The $Ni(OH)_2$/NF was immersed in the above mixed solution, and then transferred to the hydrothermal reactor and controlled at 100 °C for 24 h. After the reactor cooled down to the room temperature, taken out the NF and rinsed with water to obtain tPBA/NF.

1.5 Synthesis of PA-etched tNiFe-PBA/NF (PA-tPBA/NF)

The 74 μl PA solution was dropwise added to a beaker containing 10 mL of DI water and stirred at room temperature for 10 min. Then, a piece of tPBA/NF was put at

the bottom of the beaker and immersed into the PA aqueous solution. After 60 min, the NF was etched with PA to obtain the PA-tPBA/NF.

1.6 Synthesis of disintegrative PA-tPBA/NF (d-PA-tPBA/NF)

In order to manufacture carbon-nitrogen vacancies, the prepared PA-tPBA/NF was annealed at 200 ℃ for 4 h at a heating rate of 1 ℃ min^{-1} in a flow of N_2 (20 sccm) to obtain d-PA-tPBA/NF.

1.7 Water splitting equipment

The water splitting equipment was composed with a two-electrode system, the d-PA-tPBA/NF was used as cathode and anode, respectively. And it was driven by CHI 660D electrochemical work station, the generated O_2 and H_2 were collected by drainage collection method.

2. Characterization

The surface morphology structure of the prepared catalysts was observed by using a scanning electron microscope (SEM, JSM-7500F) and transmission electron microscopy (TEM, JEM-2100). The TD-3500 diffractometer was conducted to obtain X-ray diffraction (XRD) patterns. High-resolution transmission electron microscope (HRTEM), corresponding elemental mappings and the inset selected area electron diffraction (SAED) were also taken on the JEM-2100 with X-ray energy-dispersive spectroscopy (EDS). The X-ray photoelectron spectroscopy (XPS) data were obtained by the surface analysis instrument (Thermofisher Escalab Xi+). Raman spectra data were acquired by a DXR2 20192805. Fourier transform infrared (FTIR) spectra data were taken on Nicolet iS 10.

3. Electrochemical analysis

In a three-electrode system, the as-synthesized self-supporting catalyst was used as the working electrode and Hg/HgO electrode as reference electrode. The Pt sheet and graphite rod were used as the counter electrodes for OER and HER, respectively. The electrocatalytic performances of the catalyst were evaluated by CHI 660D electrochemical analyzer at 1.0 M KOH solution as the electrolyte. The geometric area

used for electrochemical tests is ~ 1 cm^2 for various catalysts. Before OER activity measurement, the cyclic voltammetry (CV) sweeps in the range of 0.924 V to 1.924 V vs. reversible hydrogen electrode (RHE) at a scan rate of 100 mV s^{-1} for at least 20 segments. The same operation was performed for HER between -0.776 and 0.124 V vs. RHE. The aim is to activate the catalysts until a stable CV curve is obtained. The Linear sweep voltammetry (LSV) curves for OER were collected at a scan rate of 5 mV s^{-1} between 0.924 and 2.324 V vs. RHE were corrected by 90% iR compensation, while the LSV curves were obtained for HER in the range of -0.776~0.124 V vs. RHE. The Electrochemical impedance spectroscopy (EIS) measurements were tested from 100 kHz to 0.1 Hz at an amplitude of 5 mV. To convert the measured potentials into RHE, the Nernst equation is required:

$$E_{RHE} = E_{\frac{Hg}{HgO}} + (0.059 \times pH) + 0.098 \quad \text{(S1)}$$

where the pH of 1 M KOH for testing is 13.8.

The C_{dl} was obtained by measuring the CV curves from 0.924 to 1.024 V vs. RHE at scan rates of 10-50 mV s^{-1} at an interval of 10 mV s^{-1}. The calculation formula for C_{dl} is as follows, where j_a and j_c are the current densities of the positive and negative electrodes, respectively.

$$C_{dl} = \frac{j_a - j_c}{2 \times v} \quad \text{(S2)}$$

The calculation of the electrochemical surface area (ECSA) of the sample is based on the equation:

$$ECSA = \left(\frac{C_{dl}}{C_s}\right) \times S \quad \text{(S3)}$$

where the specific capacitance (C_s) is usually between 20-60 μF cm^{-2}, and here we use 40 μF cm^{-2} according to previous research, where S represents the physical surface area of the electrode (~1.0 cm^2).

The Tafel slopes were derived from the LSV curves through the Tafel equation:

$$\eta = b \times logj + a \quad \text{(S4)}$$

where η is overpotential, j is current density and b is Tafel slope.

Turnover frequency (TOF) calculation. According to previous reports,[1] the

TOF for OER was given by:

$$TOF\ per\ site = \frac{\#\ Total\ Hydrogen\ Turn\ Overs/cm^2\ \ geometric\ area}{\#\ Surface\ Sites/cm^2\ geometric\ area} \quad \text{(S5)}$$

The total number of hydrogen turnovers was calculated from the current density using the following equation:[2]

$$\#_{H_2} = \left(j\frac{mA}{cm^2}\right)\left(\frac{1C\ s^{-1}}{1000\ mA}\right)\left(\frac{1\ mol\ e^-}{96485\ C}\right)\left(\frac{1\ mol\ H_2}{2\ mol\ e^-}\right)\left(\frac{6.022\times10^{23}H_2\ molecules}{1\ mol\ H_2}\right)$$

$$= 3.12\times10^{15}\frac{\frac{H_2}{s}}{cm^2}per\frac{mA}{cm^2} \quad \text{(S6)}$$

The total number of effective surface sites was calculated based on the following equation:

$$\frac{\#\ Surface\ sites}{cm^2\ geometric\ area} = \frac{\#\ Surface\ sites\ (flat\ standard)}{cm^2\ geometric\ area} \times Roughness\ factor \quad \text{(S7)}$$

Here, the roughness factor (*RF*) was calculated according to the following equation:

$$RF = \frac{C_{dl}(Sample)}{C_{dl}(flat\ standard)} \quad \text{(S8)}$$

Faraday efficiency (*FE*) analysis. The related experiment parameters are as follows: the geometric area of electrode is 1.0 cm^2, the applied current is 10 mA, the current density is 10 mA cm^{-2}, the temperature was set to 25 °C and the average loading weight of d-PA-tPBA/NF is 6.20 mg cm^{-2}. The drainage method was applied to measure the *FE* of OER/HER using the following equation:

$$FE(\%) = \frac{n_{exp}}{n_{theor}} \times 100 = \frac{P}{RT} \times \frac{zFV}{It} \times 100 = \frac{zFV}{ItV_m} \times 100 \quad \text{(S9)}$$

where n_{exp} and n_{theor} are the experimental and theoretical amounts of O_2/H_2 generated during the OER/HER process, respectively. V_m is the molar volume of (24.5 L mol^{-1} at 20 °C)

According to the Faraday's law, the n_{theor} was calculated by the equation:[3]

$$n_{theor} = \frac{I \cdot t}{z \cdot F}(mol) \quad \text{(S10)}$$

where I (A) is the current, t (s) is the reaction time, z is the electron transfer number and F = 96485 C mol^{-1} is the Faraday constant

According to water displacement method and ideal gas law, the n_{exp} was calculated by the equation:[3]

$$n_{exp} = \frac{p \cdot V}{R \cdot T}(mol) \quad \text{(S11)}$$

where p (Pa) is the partial pressure of O_2/H_2 produced, V (m^3) is the volume of O_2/H_2 produced per unit interval time, R = 8.314 J mol^{-1} K^{-1} is the ideal gas constant, T = 293.15 K is the reaction temperature.

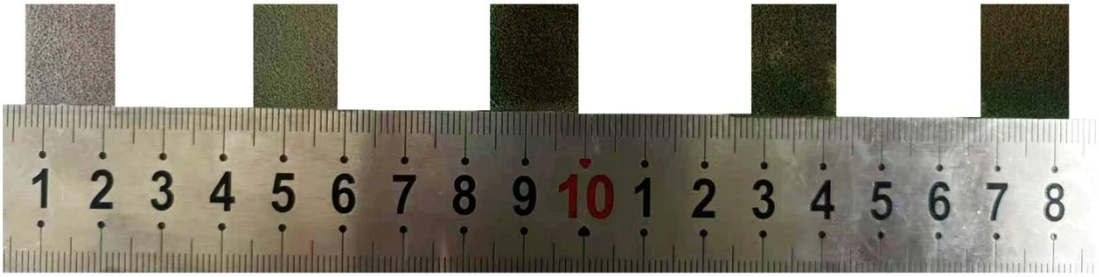

Figure S1. The optical pictures are arranged from left to right as NF, $Ni(OH)_2$/NF, tPBA/NF, PA-tPBA/NF and d-PA-tPBA/NF.

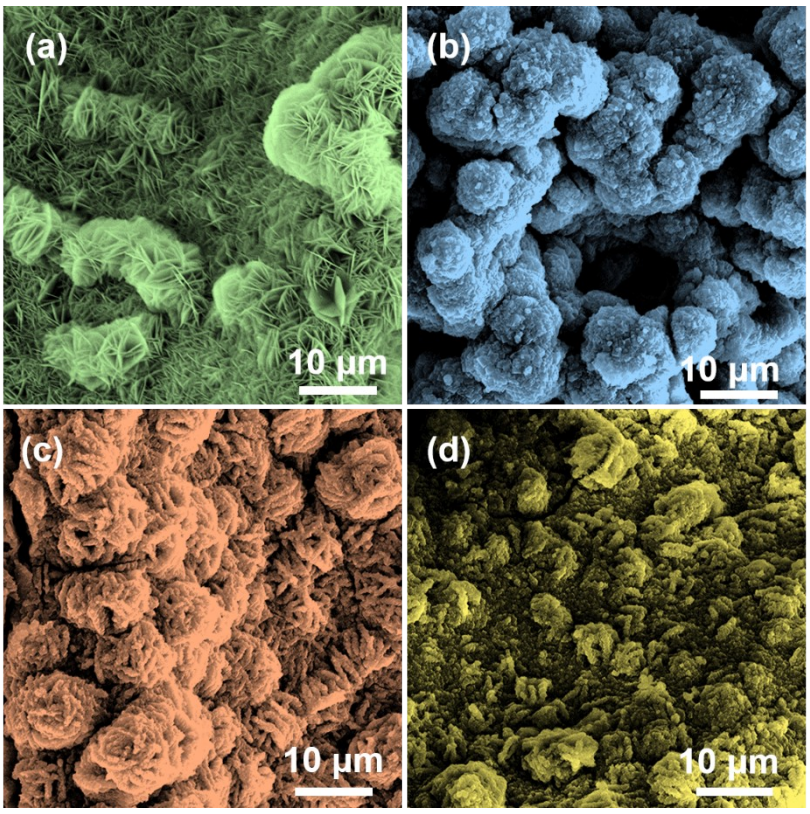

Figure S2. SEM images of (a) $Ni(OH)_2$/NF, (b) tPBA/NF, (c) PA-tPBA/NF, (d) d-PA-tPBA/NF.

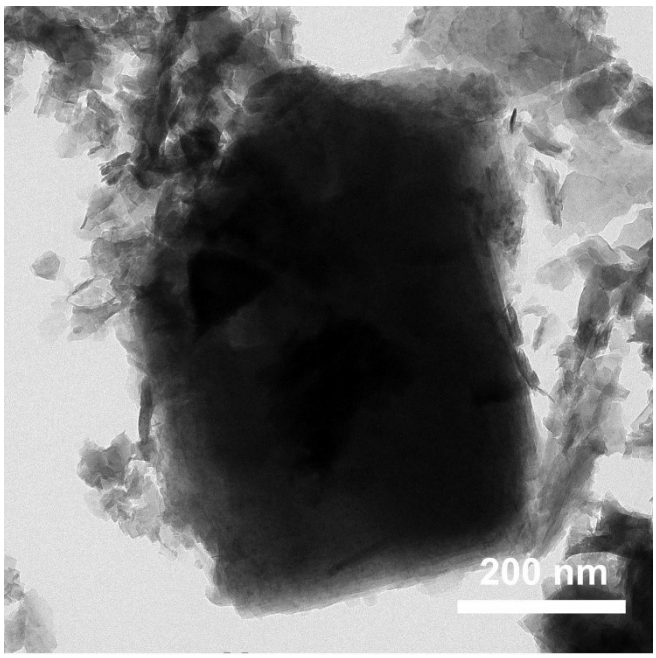

Figure S3. TEM image of d-PA-tPBA/NF with rough surface.

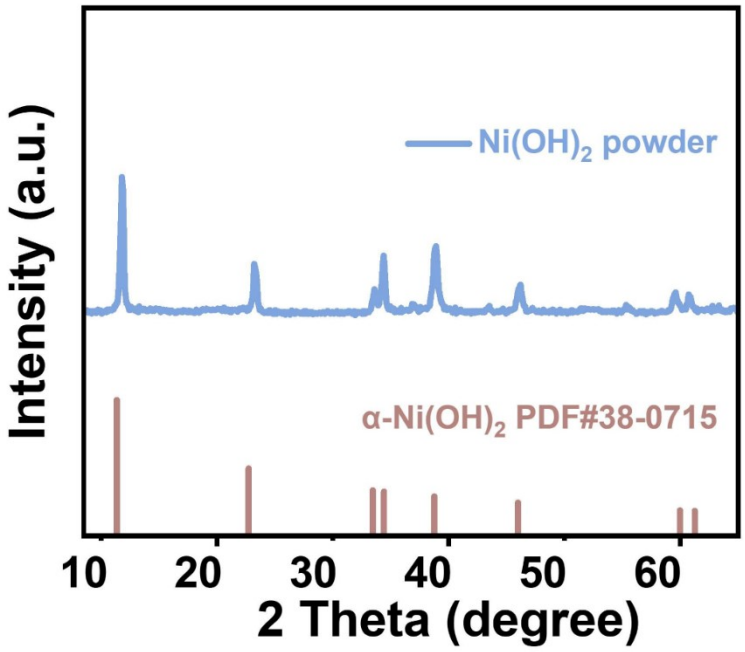

Figure S4. XRD pattern of the $Ni(OH)_2$ powder.

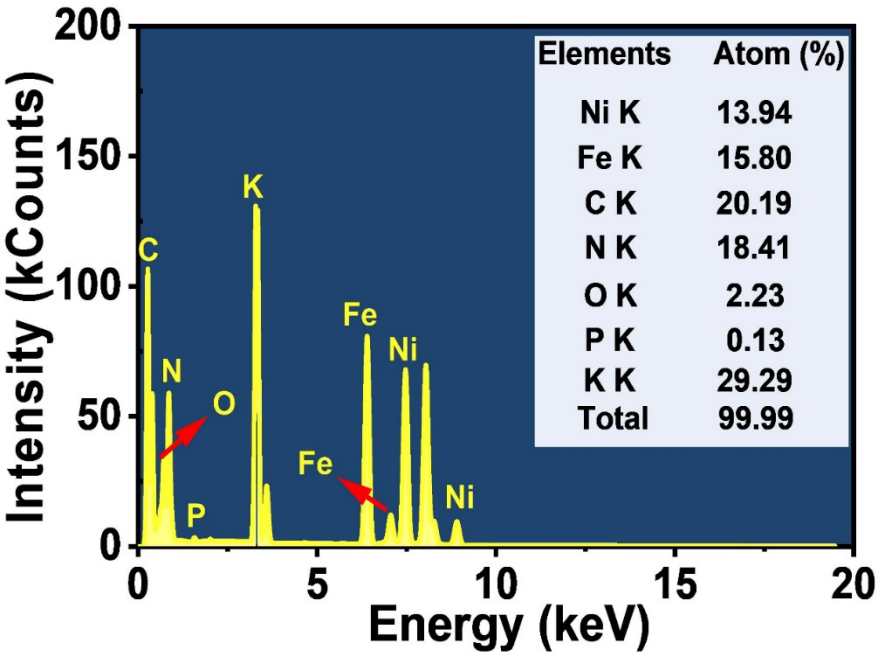

Figure S5. The EDS image of d-PA-tPBA/NF.

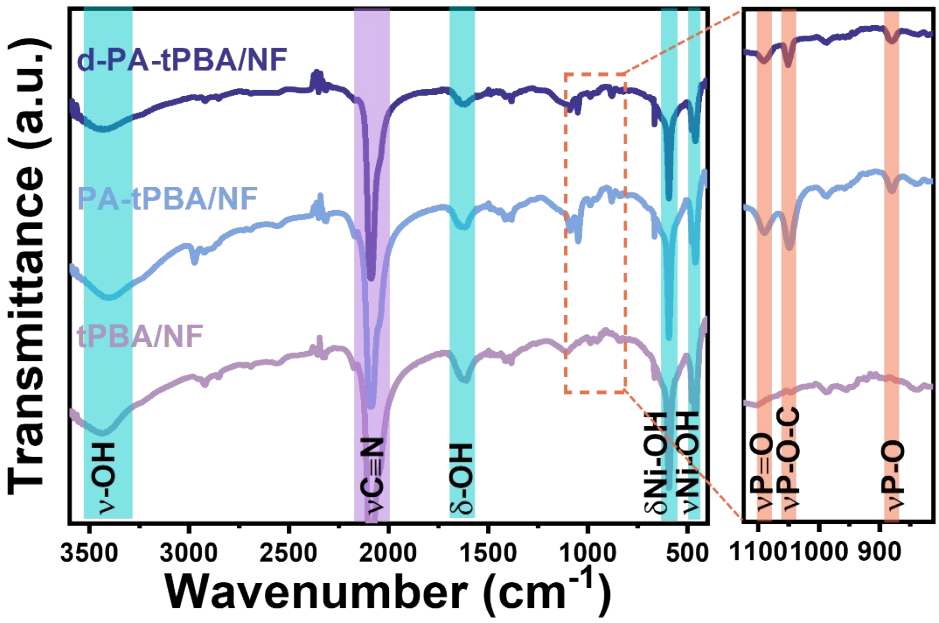

Figure S6. FTIR spectra of tPBA/NF, PA-tPBA/NF and d-PA-tPBA/NF.

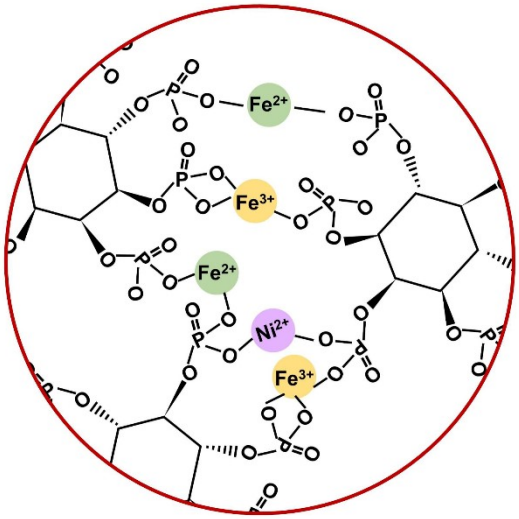

Figure S7. Schematic diagram of PA chelating metal ions.

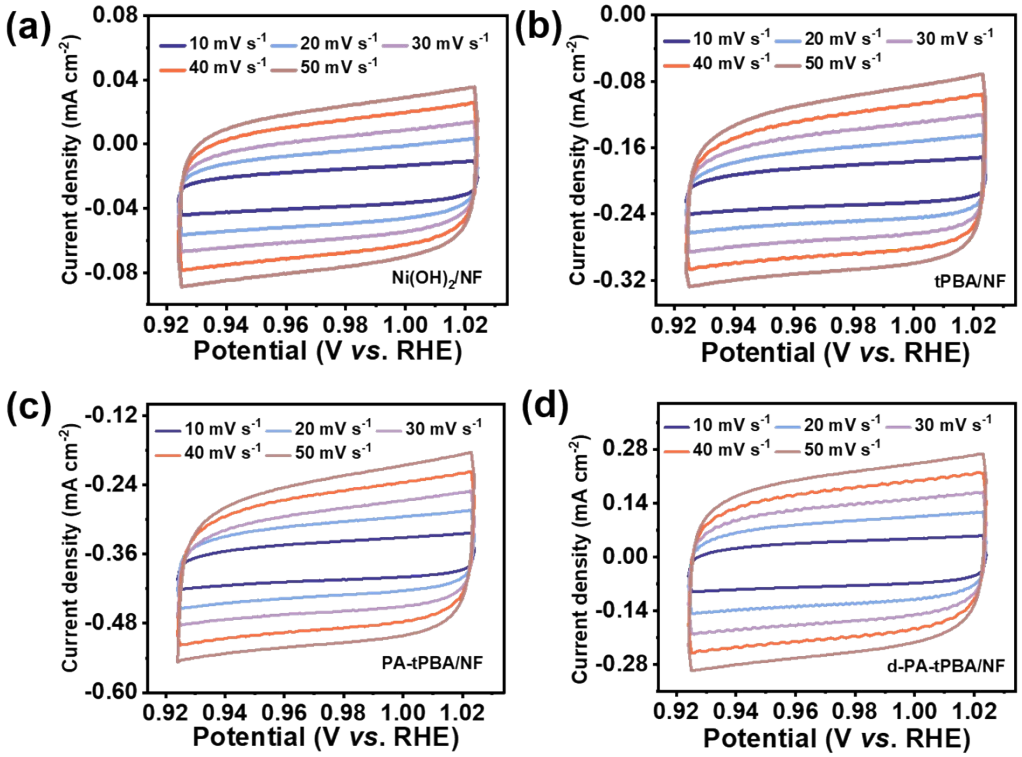

Figure S8. CV curves of (a) $Ni(OH)_2$/NF. (b) tPBA/NF. (c) PA-tPBA/NF. (d) d-PA-tPBA/NF at various scan rates (10, 20, 30, 40 and 50 mV s^{-1}) in the non-Faradic region (0.924-1.024 V vs. RHE).

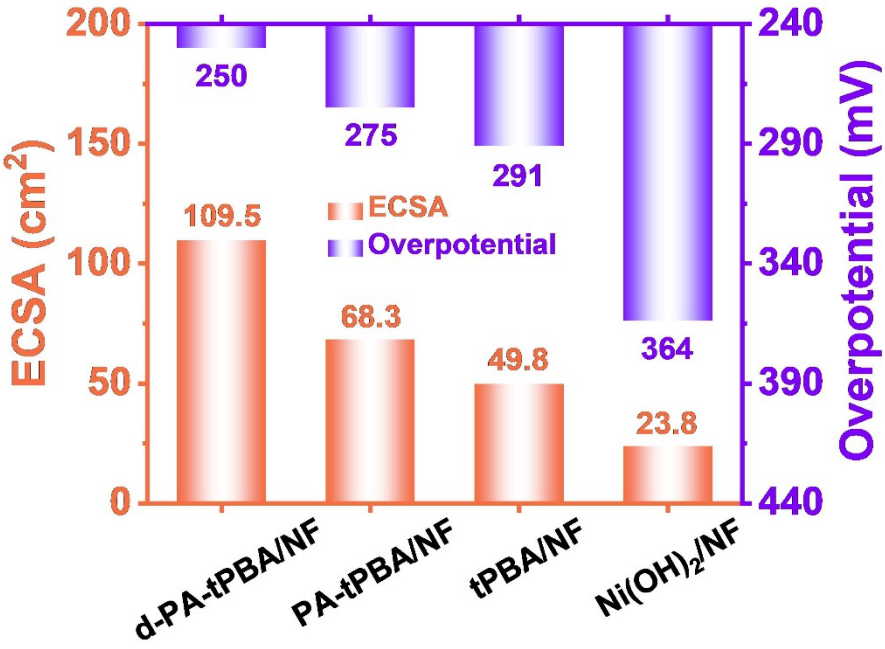

Figure S9. Double Y-axis bar chart of ECSA and overpotential at 10 mA cm^{-2} for $Ni(OH)_2$/NF, tPBA/NF, PA-tPBA/NF and d-PA-tPBA/NF.

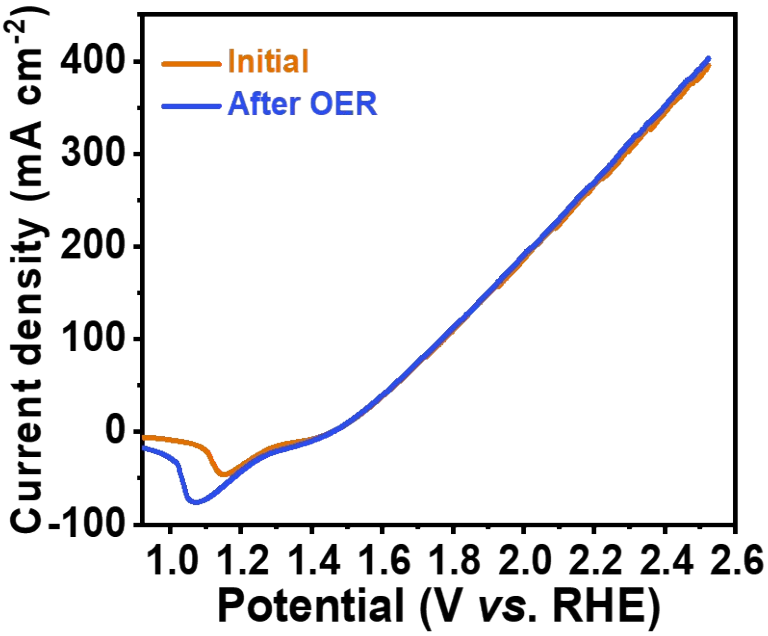

Figure S10. OER polarization curves of d-PA-tPBA/NF before and after multi-current steps.

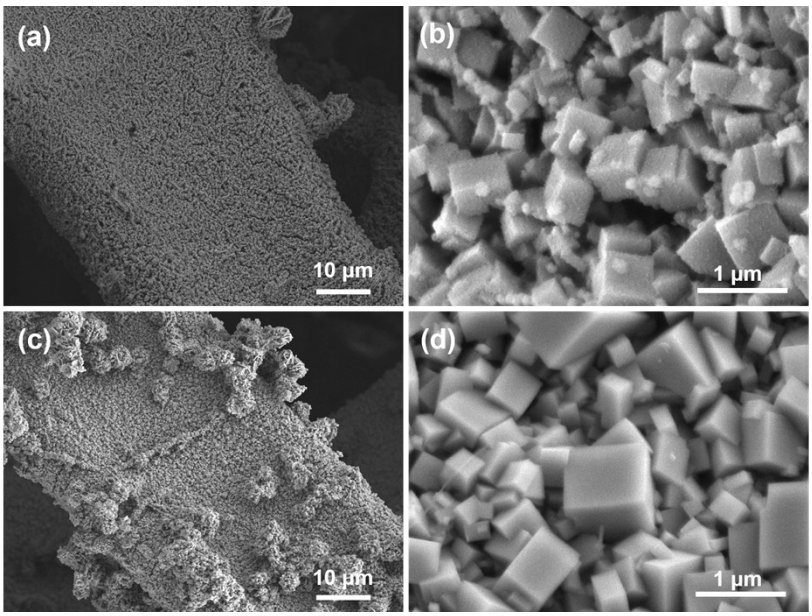

Figure S11. SEM images of d-PA-tPBA/NF after CP s for (a, b) OER and (c, d) HER.

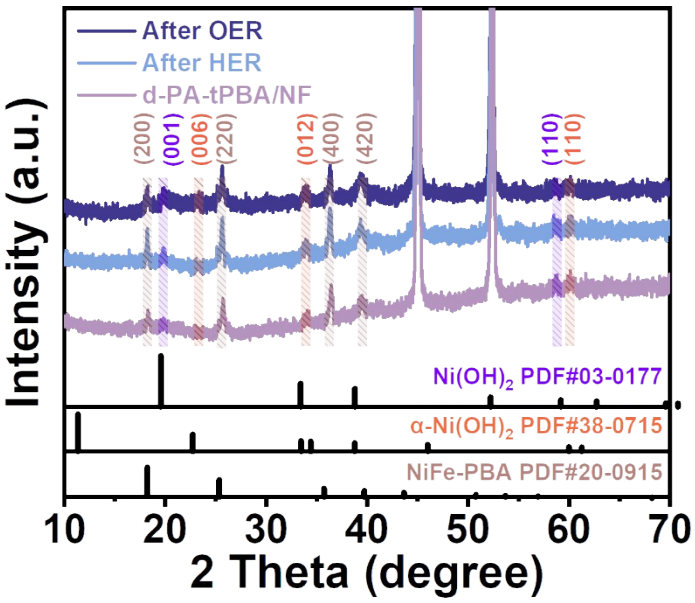

Figure S12. The XRD pattern of d-PA-tPBA/NF after 26 h CP test for both HER and OER.

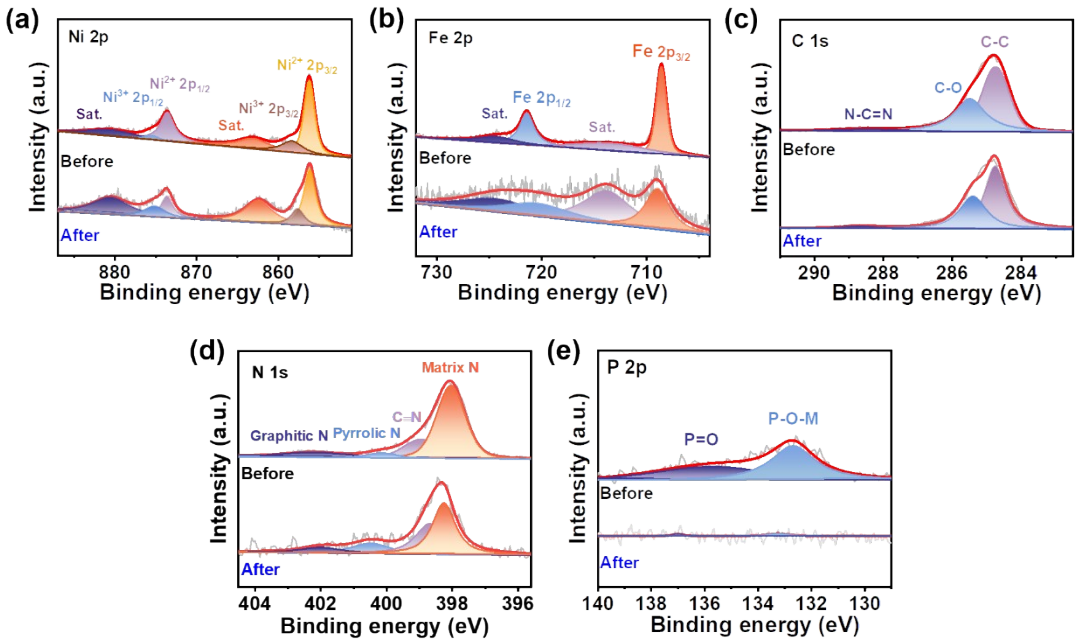

Figure S13. XPS spectrum before and after CP test for OER of d-PA-tPBA/NF. (a) Ni 2p. (b) Fe 2p. (c) C 1s. (d) N 1s and (e) P 2p.

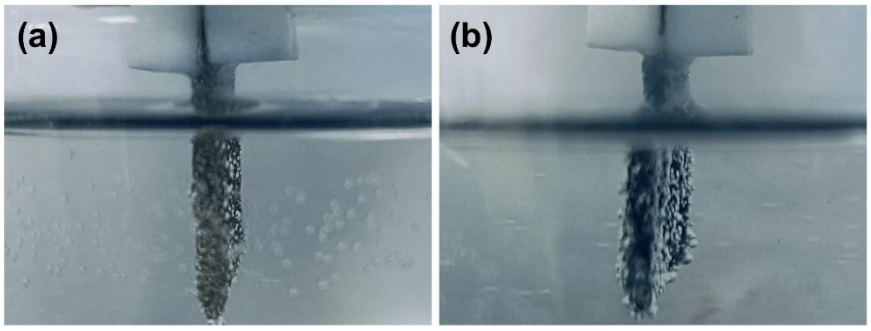

Figure S14. Surface conditions of (a) cathode and (b) anode during the overall water splitting process.

Table S1. The EIS fitting data of different catalysts at ~1.51 V vs. Hg/HgO.

Reaction	Catalysts	R_s (Ω)	R_{ct} (Ω)	CPE (F)
OER	$Ni(OH)_2$/NF	4.10	7.12	0.70
	tPBA/NF	3.99	5.62	0.82
	PA-tPBA/NF	3.86	4.16	0.99
	d-PA-tPBA/NF	3.90	3.60	1.12
HER	$Ni(OH)_2$/NF	1.71	2.62	0.87
	tPBA/NF	1.50	0.77	0.98
	PA-tPBA/NF	1.63	0.71	0.97
	d-PA-tPBA/NF	1.64	0.53	1.00

Table S2. Comparison of the key performance parameters for transition metals OER catalytic materials.

Catalysts	Overpotential η_{10} (mV)	Tafel slopes (mV dec^{-1})	Loading weight (mg cm^{-2})	References
d-PA-tPBA/NF	**η=250**	**47.9**	**6.20**	**This work**
CoZn MOF/CC	η=287	76.3	0.24	4
Co-MOF/NF	η=270	75.0	5.20	5
CoFe PBA/NF	η=256	48.0	—	6
NiCo@NiCo-PBA-AA	η=276	79.1	16.70	7
NiFe PBAs With CN vacancy	η=283	54.0	0.26	8
Co-Fe core-shell PBAs	η=271	53.7	0.13	9
MCCF/NiMn-MOFs	η=280	86.0	1.00	10
NiCo-S@ CoFe PBAs	η=268	62.0	0.15	11
Ni-Fe-S/NCQDs	η=295	85.9	1.19	12
NiFe-LDH-0.4M HMS	η=290	51.0	1.00	13

Table S3. Comparison of the overall water splitting performances of d-PA-tPBA/NF and previous reported bifunctional electrocatalysts (at 10 mA cm^{-2}) in 1 M KOH.

Catalysts	Cell voltage (V, j = 10 mA cm^{-2})	References
d-PA-tPBA/NF	**1.55**	**This work**
$Ni/Mo_2C@C$	1.55	14
$NF/H–CoMoO_4$	1.56	15
$Mo_{6.3}$-$NiSe_2$/NF	1.57	16
Ga-$NiFe_2O_4$	1.59	17
Co-Mo-B-P/CF	1.59	18
V-$NiSe_2$/NF	1.60	19
PNMO@Pi/NF	1.62	20
$Co(OH)_2$/Fe7Se_8	1.62	21
Co,V-FeNi-LDH	1.62	22
$Ce_{0.1}Ni_{0.85}Se$	1.67	23

References

1 L. Yu, L. Wu, S. Song, B. McElhenny, F. Zhang, S. Chen and Z. Ren, Hydrogen Generation from Seawater Electrolysis over a Sandwich-like NiCoN|Ni_xP|NiCoN Microsheet Array Catalyst, *ACS Energy Lett.*, 2020, **5**, 2681–2689.

2 J. D. Benck, Z. Chen, L. Y. Kuritzky, A. J. Forman and T. F. Jaramillo, Amorphous Molybdenum Sulfide Catalysts for Electrochemical Hydrogen Production: Insights into the Origin of their Catalytic Activity, *ACS Catal.*, 2012, **2**, 1916–1923.

3 D. Zhang, M. Li, X. Yong, H. Song, G. I. N. Waterhouse, Y. Yi, B. Xue, D. Zhang, B. Liu and S. Lu, Construction of Zn-doped RuO_2 nanowires for efficient and stable water oxidation in acidic media, *Nat. Commun.*, 2023, **14**, 2517.

4 J. Wu, Z. Yu, Y. Zhang, S. Niu, J. Zhao, S. Li and P. Xu, Understanding the Effect of Second Metal on CoM (M = Ni, Cu, Zn) Metal–Organic Frameworks for Electrocatalytic Oxygen Evolution Reaction, *Small*, 2021, **17**, 2105150.

5 C. Wang, H. Liu, G. Bian, X. Gao, S. Zhao, Y. Kang, J. Zhu and X. Bu, Metal-Layer Assisted Growth of Ultralong Quasi-2D MOF Nanoarrays on Arbitrary Substrates for Accelerated Oxygen Evolution, *Small*, 2019, **15**, 1906086.

6 Z. Chen, B. Fei, M. Hou, X. Yan, M. Chen, H. Qing and R. Wu, Ultrathin Prussian blue analogue nanosheet arrays with open bimetal centers for efficient overall water splitting, *Nano Energy*, 2020, **68**, 104371.

7 H. Zhang, P. Li, S. Chen, F. Xie and D. J. Riley, Anodic Transformation of a Core-Shell Prussian Blue Analogue to a Bifunctional Electrocatalyst for Water Splitting, *Adv. Funct. Mater.*, 2021, **31**, 2106835.

8 Z. Yu, Y. Duan, J. Liu, Y. Chen, X. Liu, W. Liu, T. Ma, Y. Li, X. Zheng, T. Yao, M. Gao, J. Zhu, B. Ye and S. Yu, Unconventional CN vacancies suppress iron-leaching in Prussian blue analogue pre-catalyst for boosted oxygen evolution catalysis, *Nat. Commun.*, 2019, **10**, 2799.

9 W. Zhang, H. Song, Y. Cheng, C. Liu, C. Wang, M. A. N. Khan, H. Zhang, J. Liu, C. Yu, L. Wang and J. Li, Core–Shell Prussian Blue Analogs with Compositional Heterogeneity and Open Cages for Oxygen Evolution Reaction, *Adv. Sci.*, 2019, **6**, 1801901.

10 W. Cheng, X. F. Lu, D. Luan and X. W. Lou, NiMn-Based Bimetal–Organic Framework Nanosheets Supported on Multi-Channel Carbon Fibers for Efficient Oxygen Electrocatalysis, *Angew. Chem. Int. Ed.*, 2020, **59**, 18234-18239.

11 M. Hafezi Kahnamouei and S. Shahrokhian, Mesoporous Nanostructured Composite Derived from Thermal Treatment CoFe Prussian Blue Analogue Cages and Electrodeposited NiCo-S as an Efficient Electrocatalyst for an Oxygen Evolution Reaction, *ACS Appl. Mater. Interfaces*, 2020, **12**, 16250–16263.

12 R. Wang, J. Liu, J. Xie, Z. Cai, Y. Yu, Z. Zhang, X. Meng, C. Wang, X. Xu and J. Zou, Hollow nanocage with skeleton Ni-Fe sulfides modified by N-doped carbon quantum dots for enhancing mass transfer for oxygen electrocatalysis in zinc-air battery, *Appl. Catal. B Environ. Energy*, 2023, **324**, 122230.

13 H. Zhong, T. Liu, S. Zhang, D. Li, P. Tang, N. Alonso-Vante and Y. Feng, Template-free synthesis of three-dimensional NiFe-LDH hollow microsphere with enhanced OER performance in alkaline media, *J. Energy Chem.*, 2019, **33**, 130-137.

14 D. Rathore, S. Ghosh, A. Gupta, J. Chowdhury and S. Pande, Ce-Doped NiSe Nanosheets on Carbon Cloth for Electrochemical Water-Splitting, *ACS Appl. Nano Mater.*, 2024, **7**, 9730-9744.

15 K. Chi, X. Tian, Q. Wang, Z. Zhang, X. Zhang, Y. Zhang, F. Jing, Q. Lv, W. Yao, F. Xiao and S. Wang, Oxygen vacancies engineered $CoMoO_4$ nanosheet arrays as efficient bifunctional electrocatalysts for overall water splitting, *J. Catal.*, 2020, **381**, 44-52.

16 J. Wang, Y. Su, Y. Li, H. Li, J. Guo, Q. Sun, H. Hu, Y. Liu, X. Jia, Z. Jian, L. Kong, H. Liu, J. Li, H. Chu, S. Dou and Y. Xiao, Nickel Nanoparticles Protruding from Molybdenum Carbide Micropillars with Carbon Layer-Protected Biphasic 0D/1D Heterostructures for Efficient Water Splitting, *ACS Appl. Mater. Interfaces*, 2024, **16**, 2330–2340.

17 C. Xu, G. Li, W. Huang, X. Luo, M. Wei, H. Wen, Y. Li, X. Li, Y. Zhang and W. Chen, $NiSe_2$ nanosheets with electronic structure regulated by Mo-doping as an efficient bifunctional electrocatalyst for overall water splitting, *Electrochim. Acta*, 2024, **475**, 143683.

18 S. Chen, H. Liao, X. Xu, R. Wang, Z. Sun and L. Huang, Ga-induced electronic structure

engineering of $NiFe_2O_4$ nanosheet arrays for stable and efficient oxygen evolution, *Inorg. Chem. Front.*, 2023, **10**, 6320-6328.

19 Y. Wei, P. Zou, Y. Yue, M. Wang, W. Fu, S. Si, L. Wei, X. Zhao, G. Hu and H. L. Xin, One-Pot Synthesis of B/P-Codoped Co-Mo Dual-Nanowafer Electrocatalysts for Overall Water Splitting, *ACS Appl. Mater. Interfaces*, 2021, **13**, 20024-20033.

20 M. Bai, T. Ai, W. Bao, J. Han, J. Zhang, Q. Yu, J. Liu, X. Wei, X. Zou and L. Feng, Modulating electronic structure of nickel diselenide by vanadium doping toward highly efficient and stable bifunctional electrocatalysts for overall water splitting, *J. Mater. Sci. Technol.*, 2024, **187**, 63-71.

21 R. Jiang, D. Zhao, H. Fan, Y. Xie, M. Li, H. Lin and Z. Wu, Phosphorus doping and phosphates coating for nickel molybdate/nickel molybdate hydrate enabling efficient overall water splitting, *J. Colloid Interface Sci.*, 2021, **606**, 384-392.

22 C. Gong, L. Zhao, D. Li, X. He, H. Chen, X. Du, D. Wang, W. Fang, X. Zeng and W. Li, In-situ interfacial engineering of $Co(OH)_2/Fe_7Se_8$ nanosheets to boost electrocatalytic water splitting, *Chem. Eng. J.*, 2023, **466**, 143124.

23 F. Zheng, M. A. Gaikwad, Z. Fang, S. Jang and J. H. Kim, Synergetic Engineering of Metal–Organic Framework Derived FeNi Layered Double Hydroxides for Efficient and Stable Overall Water Splitting, *Energy Fuels*, 2024, **38**, 6290-6299.